Applied Surface Science 536 (2021) 147648

Contents lists available at ScienceDirect

Applied Surface Science

journal homepage: www.elsevier.com/locate/apsusc

First-principles DFT insights into the adsorption of hydrazine on bimetallic β_1-NiZn catalyst: Implications for direct hydrazine fuel cells

Russell W. Cross, Sachin R. Rondiya, Nelson Y. Dzade*

School of Chemistry, Cardiff University, Main Building, Park Place, Cardiff, CF10 3AT Wales, United Kingdom

ARTICLE INFO

Keywords:
Bimetallic catalysts
β_1-NiZn
Fuel cells
Hydrazine
Density Functional Theory (DFT)

ABSTRACT

We present a systematic first-principles density functional theory study with dispersion corrections (DFT-D3) of hydrazine adsorption on the experimentally observed (1 1 1), (1 1 0) and (1 0 0) surfaces of the binary β_1-NiZn alloy. A direct comparison has been drawn between the bimetallic and monometallic Ni and Zn counterparts to understand the synergistic effect of alloy formation. The hydrazine adsorption mechanism has been characterised through adsorption energies, Bader charges, the *d*-band centre model, and the coordination number of the active site - which is found to dictate the strength of the adsorbate–surface interaction. The bimetallic β_1-NiZn nanocatalyst is found to exhibit higher activity towards adsorption and activation of hydrazine compared to the monometallic Ni and Zn counterparts. The Ni-sites of the bimetallic NiZn surfaces are found to be generally more reactive than Zn sites, which is suggested to be due to the higher *d*-band centre of −0.13 eV (closer to the Fermi level), forming higher energy anti-bonding states through Ni—N interactions. The observed synergistic effects derived from surface composition and electronic structure modification from Ni and Zn alloying should provide new possibilities for the rational design and development of low-cost bimetallic Ni-Zn alloy catalysts for direct hydrazine fuel cell (DHFC) applications.

1. Introduction

With the depletion of conventional energy sources and the growing need for energy in society, coupled with the challenge to ameliorate climate change, the development and improvement of safe, renewable, and low-cost clean energy technologies are necessary. The development of fuel cells has attracted significant attention recently owing to their promising potential to provide a clean and possibly sustainable energy generation [1,2]. Currently, the Proton Exchange Membrane (PEM) fuel cell is highly developed, however, there are many inherent safety and practical problems such as the production, storage, and distribution of hydrogen that still present strong limitations for industrial-scale applications [3–6]. In recent years, the direct hydrazine fuel cell (DHFC) has gained significant research interest because of the high power density and therefore has promising application for the automotive industry [7–9]. DHFC is a carbon-free process and has the potential to output a power generation performance of 0.5 W cm^{-2} and a cell voltage of 1.56 V, which is comparable to the PEM fuel cell [10,11]. However, its full implementation is hindered by the lack of highly efficient, stable and inexpensive catalysts. Other suggestions for using hydrazine towards an environmentally friendly economy include its potential as a hydrogen storage material, via its decomposition pathway:

$$N_2H_4 \rightarrow 2H_2 + N_2$$

This is a competitive pathway with the decomposition to ammonia – with the route depending upon whether the N—N or N—H bonds of hydrazine are broken first [12].

Ni-based catalysts - non-noble metal alternatives to platinum have been shown to be active for each of these processes. Hydrazine decomposition has been shown on Ni-nanofibres when supported on carbon nanotubes by Ding, Lin, and Guo - achieving 100% selectivity towards hydrogen [13]. Researchers at the Dihastu Motor Company have also shown that carbon supported-Ni was active for the DHFC, showing good selectivity and low amounts of ammonia production [14]. Unfortunately, Ni-nanoparticles suffer from atom run-off, hence dramatically lowering the activity of the monometallic catalysts [15]. Bimetallic catalysts can be formed to overcome these issues, as Ni has an innate ability to produce alloyed systems with other transition metals [16]. Ni-based bimetallic heterogeneous catalysts often show new and improved activity and stability towards their respective reactions - such as Ni-Rh [17], Ni-Ir, [18,19] or Ni-Pt [20–22] - which show marked improved activity for hydrazine decomposition. However, avoiding expensive and less abundant noble metals is necessary if we

* Corresponding author.
E-mail address: DzadeNY@cardiff.ac.uk (N.Y. Dzade).

https://doi.org/10.1016/j.apsusc.2020.147648
Received 30 June 2020; Received in revised form 6 August 2020; Accepted 22 August 2020
Available online 28 August 2020

are to achieve widespread, sustainable commercialisation of DHFC technology. Promising non-noble bimetallic catalysts for DHFC's include alloys with other first row transition metals, such as Ni-Cu, [23] Ni-Fe, [24] and particularly Ni-Zn [25,26]. Recently, Feng et al. [27] synthesised an Ni-Zn catalyst combined with a reduced graphene oxide layer, finding this gave almost 100% selectivity towards hydrazine electro-oxidation in the DHFC. The catalyst also showed good stability over time, hence improving substantially on the monometallic Ni-catalyst. Atanassov et al. [11] have also found NiZn catalysts to be active for DHFC's when supported on Ketjenblack, a carbon-based support material. As a result, the surface area of the catalyst was increased, leading to higher contact times with hydrazine, thereby increasing the activity.

Hydrazine adsorption onto the bimetallic Ni-Zn catalyst surface would precede any reactions that take place inside the DHFC or any decomposition routes, as such, understanding of the strength and features of adsorption of hydrazine onto the catalyst surface is essential for the successful development of efficient bimetallic Ni-Zn catalysts in these areas. The fundamental aspects of hydrazine adsorption, including the initial adsorption geometries, adsorption energies, structural parameters, and electronic properties, are deemed vital for the rational design of improved Ni-Zn catalysts. Detailed information is, however, difficult to obtain directly from experiments and the underlying physical driving forces that control the reactivity of hydrazine with the bimetallic Ni-Zn surfaces remain not fully understood. First-principles density functional theory (DFT) calculations provide an alternative way to gain fundamental insight, as it is capable of accurately predicting lowest-energy adsorption geometries and identifying charge transfer and further electronic effects [28–31]. DFT-based calculations have been employed extensively to predict the adsorption geometries of hydrazine on metallic surfaces and offers good insight into catalyst activity [24,32,33]. Previous DFT work has been done on the Ni-Zn alloy, although the specific factors behind how hydrazine adsorbs are yet unknown [33].

In the present study, dispersion-corrected DFT-D3 calculations are employed to comprehensively investigate the adsorption properties of hydrazine on the bimetallic β_1-NiZn alloy catalyst (1 0 0), (1 1 0), and (1 1 1) surfaces. Insights into the synergistic beneficial effects of Ni-Zn alloying was derived by drawing a comparison between the hydrazine adsorption energetics and mechanisms on the bimetallic NiZn surfaces to the monometallic Ni(1 1 1) and Zn(0 0 1) surfaces. The energetics and structural parameters of the lowest-energy adsorption configurations of the hydrazine are presented and a *d*-band model was developed to gain insight into the differences in reactivity of the bimetallic catalyst compared to the monometallic counterparts. Differential charge density *iso*-surface contour and projected density of states analyses were carried out to gain further atomic-level insights into the hydrazine adsorption mechanism.

2. Computational details

The optimized surface and adsorption structures were determined using the plane-wave-based DFT method, implemented in the Vienna Ab-Initio Simulation Package (VASP) [34–36]. The interactions between the valence electrons and the ionic core were described with the projected augmented wave (PAW) method [37,38]. The electronic exchange–correlation potential was treated using the Perdew-Burke-Ernzerhof (PBE) functional [39]. A high energy cut-off of 600 eV was used for the plane-wave basis sets, with a convergence criterion set to 10^{-6} eV between two ionic steps for the self-consistency process. The Brillouin zone was sampled with a Monkhorst-Pack [40] k-point grid of 5 × 5 × 5 for bulk Ni, Zn, and NiZn, while for geometry optimisation of cleaved surfaces, a k-point grid of 3 × 3 × 1 was used.

The low miller index surfaces of β_1-NiZn were created from the relaxed bulk material using the METADISE code [41], which ensures the creation of surfaces with zero dipole moment perpendicular to the surface plane. The surfaces were modelled using the slab model and for each surface a slab thickness of at least 10 Å was increased until convergence of the surface energy was achieved within 1 meV per cell. In each simulation cell, a vacuum region of 15 Å was tested to be sufficient to avoid interactions between periodic slabs in the z-direction. From the full geometry relaxation of each surface we have calculated the surface energy (γ), which is the energy required to cleave an infinite crystal in two along a given crystallographic plane using the relation:

$$\gamma = \frac{E_{surface} - nE_{bulk}}{2A}$$

where $E_{surface}$ is the energy of the naked surface, n is the number of repeating unit cells in the z-direction, E_{bulk} is the energy of the bulk system, A is the surface area of the relaxed system - where the factor of 2 reflects the fact that there are two surfaces for each slab with identical atomic ordering at the bottom and top layers.

The hydrazine adsorption calculations were carried out on a 3 × 3 supercell of the bimetallic NiZn (1 1 1), (1 1 0) and (1 0 0) surfaces, which are large enough to minimize the lateral interactions between the hydrazine molecules in neighbouring image cells. The structural optimizations of Ni-Zn systems were carried out without any symmetry constraint and the hydrazine molecule was free to move away laterally and vertically from the initial binding site or reorient itself to find the minimum energy adsorption structure. To determine the optimum adsorption sites and geometries, the hydrazine molecule and the topmost three layers of each surface slab are allowed to relax unconstrainedly until residual forces on all atoms had reached 0.03 eV $Å^{-1}$. Van der Waals dispersion forces were accounted for by utilising the Grimme DFT-D3 functional [42], which adds a semi-empirical dispersion correction to the conventional Kohn-Sham DFT method. This is important because standard DFT calculations fail to provide an accurate description of the asymptotic decreasing behaviour of the long-range vdW interactions that are ubiquitous in hybrid inorganic/organic systems [43–45]. Previous studies have shown that the inclusion the dispersion correction have led to proper description of the hydrazine adsorption structures and energetics on metallic Ni and Cu surfaces [32,46,47]. To quantify the hydrazine adsorption strength on the NiZn surfaces, the adsorption energy (E_{ads}) was calculated using the following equation:

$$E_{ads} = E_{System}^{PBE+D3} - (E_{Surface}^{PBE+D3} + E_{Adsorbate}^{PBE+D3})$$

where E_{System}^{PBE+D3} is the energy of the adsorbed hydrazine to the catalyst slab, $E_{Surface}^{PBE+D3}$ is the energy of the naked surface and $E_{Adsorbate}^{PBE+D3}$ is the energy of the adsorbate in the gas phase. Therefore, a negative E_{ads} value indicates an exothermic, favourable adsorption, whereas a positive value indicates an endothermic, and less favourable adsorption.

The *d*-band centre (E_d) was calculated for each surface using the relation:

$$E_d = \frac{\int_{-\infty}^{\infty} E \cdot D(E) dE}{\int_{-\infty}^{\infty} D(E) dE}$$

where E_d is the *d*-band centre and D(E) are the density of states (DOS) for the surface atoms. The *d*-band centre is a useful descriptor as the Fermi level of transition metals originates primarily from the *d*-orbitals. Hybridisation between surface orbitals and adsorbates forms bonding and anti-bonding states. A higher *d*-band centre is therefore associated with higher energy anti-bonding states and hence, stronger adsorption.

3. Results and discussion

3.1. Bulk and surface characterization of NiZn catalyst

The bulk β_1-NiZn was modelled in the tetragonal crystal structure, as shown in Fig. 1a. The fully optimized lattice parameters are predicted at a = b = 2.686 Å, and c = 3.262 Å in good agreement with previous experimental results of a = b = 2.75 Å and c = 3.21 Å [48].

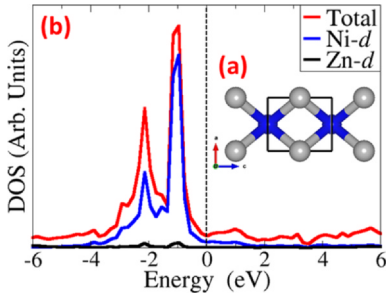

Fig. 1. The NiZn unit cell is shown ((a), inset), where Ni-atoms are blue, and Zn-atoms are silver. The partial density of states (PDOS) for the bulk NiZn material showing the contributions from the Ni-*d* (blue line) and Zn-*d* (black line) to the total DOS (red line) (b) (For interpretation of the references to colour in this figure legend, the reader is referred to the web version of this article.).

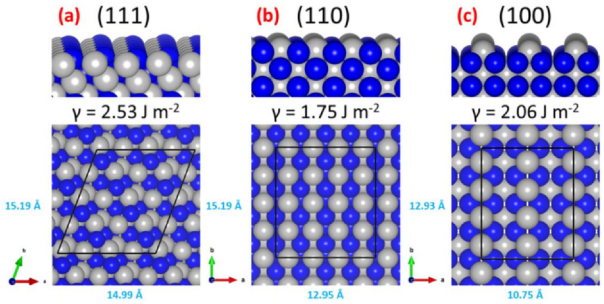

Fig. 2. Side and top views of (a) (111), (b) (110) and (c) (100) surfaces of bimetallic NiZn catalyst, with surface energies and supercell sizes displayed.

Fig. 3. Wulff-constructed equilibrium morphology of bimetallic NiZn nanoparticle.

The partial density of states (PDOS) shown in Fig. 1b reveals the metallic conductivity of the alloy, with the Ni-*d* orbitals dominating states surrounding the fermi level, in agreement with earlier DFT results [33]. From the optimized bulk NiZn material, the (100), (110), and (111) surfaces were created and fully relaxed in order to determine their relative stabilities (Fig. 2). The surface energies of the (100), (110), (111) surfaces are calculated at 2.06, 1.75, and 2.53 J m^{-2} respectively, which indicates that the order of decreasing stability is (110) < (100) < (111). The differences in the stabilities can be attributed to differences in the surface terminations and the coordination numbers of the topmost surface atoms. The (110) surface is terminated by Ni:Zn in a 1:1 ratio, with the Ni and Zn atoms in an 8-fold coordination number (CN). The (111) surface is also terminated by Ni and Zn, but in a 1:2 ratio, with the surface Ni atoms having coordination number of 6. The (100) surface on the other hand is terminated by a Zn-ad-atom having 5-fold coordination, with accessible Ni-sites below with higher coordination. Based on the calculated surface energies, we have simulated the equilibrium crystal morphology of the NiZn nanoparticle using Wulff construction [49–51]. As shown in Fig. 3, all three surfaces are expressed in the NiZn nanoparticle with the (110) covering the largest area, in line with it being the most thermodynamically stable.

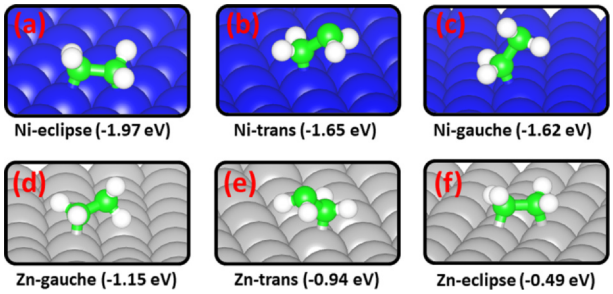

Fig. 4. Lowest-energy adsorption structures of hydrazine on Ni(111)-(a-c) and Zn(001)-(d-f) surfaces. Colour code: blue = Ni, silver = Zn, green = N and white = H. Below each image are their respective geometries and adsorption energies. (For interpretation of the references to colour in this figure legend, the reader is referred to the web version of this article.)

3.2. Hydrazine to the monometallic Ni(111) and Zn(001) surfaces

Prior to investigation the adsorption of hydrazine on the bimetallic NiZn surfaces, the adsorption process has been systematically characterized on the monometallic Ni(111) and Zn(001) surfaces for comparison. Hydrazine in the gas phase has been found to adopt the gauche formation [52]. This is due to the hyper conjugate mechanism, which minimises repulsion between the lone pairs of each nitrogen by rotation about the N—N axis [53]. Consequently, the relative energies of the eclipsed and trans geometries are higher than gauche in the gas phase [54].

Shown in Fig. 4a-c are the lowest-energy gauche, trans, and eclipsed adsorption configurations of hydrazine on the monometallic Ni(111) surface, with the characteristic binding energies and structural parameters given in Table 1. The gauche, trans, and eclipsed binding configurations released adsorption energies of −1.62, −1.65, and −1.97 eV, respectively. This indicates that the eclipsed binding mode, wherein both N atoms interact with adjacent Ni sites, is the most stable binding geometry on the Ni(111) surface. The surface Ni-N bond distances in the most stable eclipsed geometry are calculated at 1.996 and 2.011 Å, with hydrazine's N—N bond converged at 1.440 Å. For the monodentate trans and gauche adsorption configurations, the interacting Ni-N bond distance is calculated at 1.965 and 2.012 Å, respectively, whereas the N—N bonds are converged at 1.457 and 1.441 Å. Bader population analysis revealed that the hydrazine molecule is oxidised to only a small extent, characterized by loss of charge to the interacting surface species. The hydrazine molecule lost 0.108, 0.171, and 0.178 e^- to the surface when adsorbed in the gauche, trans, and eclipsed configurations, respectively. Although small, the loss in electron density resulted in structural modification (internal rotation) of the hydrazine molecule with the dihedral angle reduced to 37.1° in the eclipsed adsorption geometry, compared to the gas phase gauche conformer dihedral angle of 91.0°. This disturbance of the hyper conjugate

Table 1
Adsorption energy (E_{ads}) and geometric data for hydrazine adsorption to the monometallic Ni(111) and Zn(001) catalyst surfaces. θ is the dihedral angle between the two NH_2 units of hydrazine. $\Delta q(N_2H_4)$ is the net Bader charge of adsorbed hydrazine.

Surface	Configuration	E_{ads}/eV	d(surf-N)/Å	d(N—N)/Å	θ/°	$\Delta q(N_2H_4)/e^-$
Ni(111)	Eclipse	−1.97	2.011, 1.996	1.440	37.1	0.178
	Trans	−1.65	1.965	1.457	176.8	0.171
	Gauche	−1.62	2.012	1.441	94.4	0.108
Zn(001)	Gauche	−1.15	2.196	1.428	98.8	0.047
	Trans	−0.94	2.142	1.461	179.9	0.062
	Eclipse	−0.49	2.267, 2.280	1.453	26.3	0.086

mechanism has also been observed on several other metallic surfaces, such as hydrazine adsorption to Pt(1 1 1) [53]. The N—N distance of 1.440 Å also shows a minute change from the gas phase species, 1.441 Å, hence presenting suitability towards the DHFC and decomposition mechanisms by reducing ammonia formation through the N—N bond cleavage mechanism and favouring N_2 production [18,55].

Compared to the Ni(1 1 1) surface, the gauche, trans and eclipsed adsorption configurations of hydrazine on the monometallic Zn(0 0 1) surface (Fig. 4d-f) released lower adsorption energies of −1.15, −0.94, and −0.49 eV, respectively, indicating that the Ni(1 1 1) surface is more reactive towards hydrazine adsorption than the Zn(0 0 1) surface. In the most stable gauche geometry, the Zn-N adsorbate–surface bonds and N—N hydrazine bonds are predicted at 2.196 and 1.428 Å, respectively. In the trans and eclipsed adsorption configurations the interacting Zn-N bond distance is predicted at 2.142 and 2.267 Å, respectively, whereas the N—N bond length is converged to 1.461 and 1.453 Å. Similar to the Ni(1 1 1), the hydrazine is only slightly oxidized upon adsorption on the Zn(0 0 1) surface: the hydrazine molecule lost a charge of 0.047, 0.062, and 0.086 e^- to the interacting surface species when adsorbed in the gauche, trans, and eclipsed configurations, respectively. The dihedral angle is predicted at 98.8, 179.9, and 26.3° for the gauche, trans and eclipsed adsorption configurations at the Zn(0 0 1) surface. The smaller changes in the dihedral angles, along with the extremely small Bader charge transfers indicate only minor disruption in the hyper conjugate mechanism. Considering that stronger adsorption is correlated with high activity [33], the weaker hydrazine adsorption on the Zn(0 0 1) compared the Ni(1 1 1) surface suggest that the monometallic Zn(0 0 1) may be inappropriate for the DHFC applications. This is consistent with the work of Wang et al. [25], who found Zn-film to be inactive for the DHFC.

3.3. Hydrazine adsorption to the bimetallic NiZn catalyst

As for the monometallic Ni and Zn catalysts, hydrazine has been adsorbed onto the bimetallic NiZn (1 0 0), (1 1 0), and (1 1 1) surfaces in the gauche, trans, and eclipsed conformations. The lowest-energy adsorption geometries are displayed in Fig. 5 and the optimized structural parameters are summarized in Table 2. For the NiZn(1 1 1)-hydrazine interactions, the eclipsed geometry (Fig. 5a) has been found to be the most stable, with a highly exothermic adsorption energy of −2.71 eV. In the eclipsed structure, hydrazine is bound to adjacent Ni and Zn sites, with the Ni—N and Zn—N bond distances calculated at 2.032 and 2.136 Å, respectively. As shown by the dihedral angle, the hydrazine NH_2 units are not fully aligned to 0°, as for gas-phase eclipsed, but to 35.0°, indicating that hydrazine has not been fully oxidised and some repulsion between the two N-lone pairs remains. Consistent with this, our Bader population analysis shows a lesser extent of oxidation (Δq (N_2H_4) = 0.128 e^-) compared to the eclipsed geometry on the monometallic Ni(1 1 1) surface ($\Delta q(N_2H_4)$ = 0.178 e^-). Although these differences are small, it is enough to favour the eclipsed formation. The high binding energy is attributed to the low-coordinated Ni atoms present on the surface (CN = 6), strengthening the surface-hydrazine interactions. The second most stable hydrazine binding geometry on the NiZn(1 1 1) surface is a monodentate trans configuration (Fig. 5b), also releasing a high adsorption energy of −2.25 eV. In the adsorbed trans geometry, the dihedral angle calculated at 173.4° is relatively close to that of the gas phase trans configuration (180.0°). The N—N bond is somewhat activated, as reflected in the small increase in the N—N distance from 1.468 to 1.491 Å. —The gauche adsorption configuration on the NiZn(1 1 1) surface (Fig. 5c) released the lowest adsorption energy, calculated at −1.99 eV. In the gauche configuration, hydrazine adsorbs atop a single Ni-site with the Ni—N, N—N bond lengths, and dihedral angle predicted at 1.960 Å, 1.450 Å, and 106.4°, respectively. The generally stronger binding of hydrazine to the bimetallic NiZn (1 1 1) surface compared to the monometallic Ni(1 1 1) and Zn(1 0 0) surfaces indicates that the Ni-Zn alloy presents a more active site for hydrazine activation, which results from the synergistic effects between the two metals.

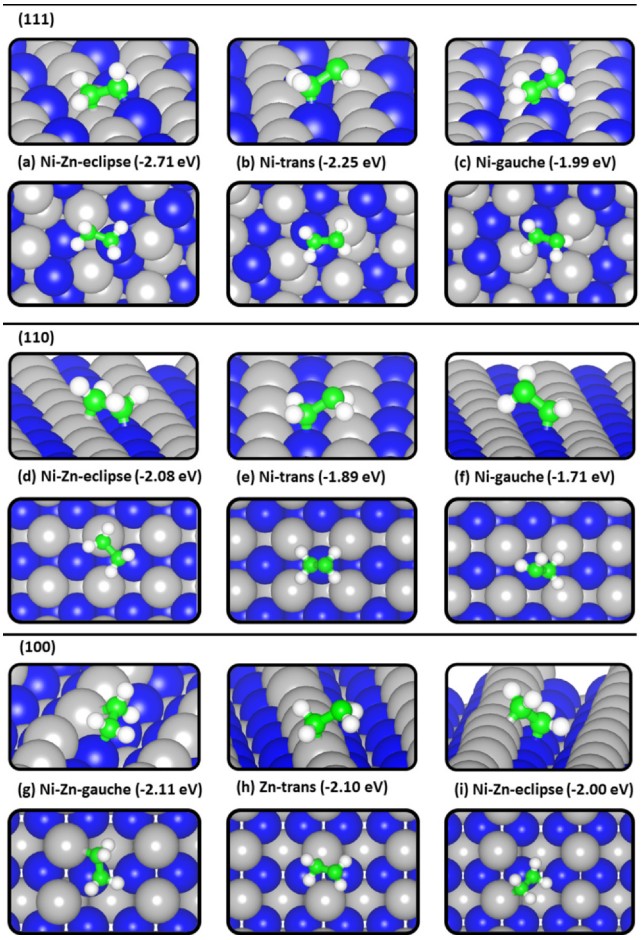

Fig. 5. Side (top) and top (down) views of the lowest-energy adsorption structures of hydrazine on bimetallic NiZn (1 1 1)-(a-c), (1 1 0)-(d-f) and (1 0 0)-(g-i) catalyst surfaces. Colour code: blue = Ni, silver = Zn, green = N and white = H. Alongside each image is their respective geometries and adsorption energies.

For the NiZn(1 1 0)-hydrazine interactions (Fig. 5d-f), the preferred adsorption configuration is predicted to be the eclipsed geometry, wherein the hydrazine binds via both N atoms at adjacent Ni and Zn sites (Fig. 5d), releasing an adsorption energy of −2.08 eV. The Ni—N, Zn—N, and N—N distances are calculated at 2.016, 2.179, and 1.472 Å, respectively. The dihedral angle is predicted to be closer to zero (θ = 8.7°) than atop the NiZn(1 1 1) surface, where the dihedral angle is predicted at 35.0°. This may partly be attributed to the differences in the surface structure as the NiZn(1 1 0) surface has a flat topology, with the N—N axis contorted to allow adsorption to adjacent surface sites. However, the coordination number of the surface Ni and Zn both stand at 8 on NiZn(1 1 0), compared to 6 and 7, respectively, on the NiZn (1 1 1) surface. Hence, a lower adsorption energy is observed for NiZn (1 1 0) as shown from bond order conservation theory [56]. Compared to the most stable bidentate eclipsed geometry, the monodentate trans and gauche configurations at Ni top sites on the NiZn(1 1 0) surface released adsorption energies of −1.89 and −1.71 eV, respectively. The Ni—N and N—N distances are calculated at 2.000 and 1.464 Å, for the trans geometry and at 2.022 and 1.448 Å the for gauche geometry. Minor oxidation occurs in hydrazine for both the trans and gauche conformations and leads to an adsorption structure similar to that of the respective gas-phase species. This is shown by the dihedral angle of 177.1 and 104.0° for the trans and gauche systems.

The bimetallic NiZn(1 0 0) surface is terminated in Zn ad-atoms and

Table 2
Adsorption energies (E_{ads}) and geometric data for hydrazine adsorption to the bimetallic NiZn (1 1 1), (1 1 0) and (1 0 0) surfaces. $\Delta q(N_2H_4)$ is the net bader charge of adsorbed hydrazine.

Surface	Configuration	E_{ads}/eV	d(Ni−N)/Å	d(Zn−N)/Å	d(N−N)/Å	θ/°	$\Delta q(N_2H_4)/e^-$
NiZn(1 1 1)	Eclipse	−2.71	2.032	2.136	1.451	35.0	0.1278
	Trans	−2.25	1.936	–	1.468	173.4	0.1485
	gauche	−1.99	1.960	–	1.450	106.4	0.1079
NiZn(1 1 0)	Eclipse	−2.08	2.016	2.179	1.472	8.7	0.1345
	Trans	−1.89	2.000	–	1.464	177.1	0.0609
	Gauche	−1.71	2.022	–	1.448	104.0	0.0726
NiZn(1 0 0)	Gauche	−2.11	2.024	2.342	1.443	63.4	0.0338
	Trans	−2.10	–	2.334	1.469	146.8	0.0569
	Eclipse	−2.00	1.989	2.184	1.439	14.8	0.0577

hence exhibits adsorption trends akin to the monometallic Zn(0 0 1) surface. Low-coordinated Zn sites dominate the NiZn(1 0 0) surface (CN = 5) and as a result the gauche adsorption has been found to be the most stable (Fig. 5g). The bidentate gauche adsorption geometry released an adsorption energy of −2.11 eV, with the Ni-N and Zn-N distances converged at 2.024 and 2.342 Å, respectively. Although the gauche adsorption is favoured here, as for Zn(0 0 1), the adsorption energy and interaction is much stronger, owing to the synergistic effect between Ni and Zn in the alloy. The geometry has been ascribed to be gauche, however, the dihedral angle of 63.4°, shows it lies between an eclipsed and gauche formation. The top-most NH_2 unit has rotated in order to align its lone pair with the low-coordinated Zn atoms, hence stabilising the system. This is consistent with the inability of Zn sites to bind to hydrazine efficiently. The trans (Fig. 5h) and eclipsed (Fig. 5i) configurations released adsorption energies of −2.10 and −2.00 eV, respectively. In both geometries, the hydrazine molecule is only marginally oxidized as reflected in the Bader charges reported in Table 2. The less stable hydrazine adsorption structures and energetics at Zn-sites on the (1 1 1) and (1 1 0) NiZn surfaces are shown in Supporting Information Fig. S1 and Table S1.

Modification of the *d*-band centre resulting from the synergistic effects between the two metals is another origin of the differences in reactivity of the bimetallic NiZn surfaces compared to the monometallic. Since the adsorbate interaction to the metal surface occurs via the N-lone pair (N-*p*) and surface metal *d*-states, the bonding interaction creates a set of bonding and anti-bonding states. The energetic level of these is then defined by the *d*-band centre as the anti-bonding states are less occupied when the *d*-band centre is closer to the Fermi level due to their resulting higher energy [57]. To probe the electronic effects of NiZn surface reactivity, the *d*-band centres (E_d) for each surface Ni and Zn sites have been analysed [56–58]. A plot of the calculated E_d values for the Ni(1 1 1), Zn(0 0 1), NiZn(1 1 1), (1 1 0) and (1 0 0) surfaces is shown schematically in Fig. 6a. The *d*-band centre projected on Ni-atoms of Ni(1 1 1) and Zn-atoms of Zn(0 0 1) surface is predicted at −1.65 eV and −7.14 eV, respectively (Fig. 6b and c). The weaker binding of hydrazine on Zn(0 0 1) compared to Ni(1 1 1) can thus be attributed to the higher *d*-band centre and formation of higher energy antibonding orbitals for Ni(1 1 1), causing them to be less filled [59]. Compared to the monometallic surfaces, E_d of Ni and Zn atoms of the bimetallic NiZn surfaces has shifted closer to the Fermi level from each respective monometallic counterpart (Fig. 6d-f). The Ni *d*-band shifts from −1.65 eV for Ni(1 1 1) to −0.91, 1.13, and −0.99 eV for NiZn (1 1 1), (1 1 0) and (1 0 0), respectively. Similarly, the Zn *d*-band centre shifts from −7.14 eV of the Zn(0 0 1) to −6.51, −6.74 and −6.60 eV for the NiZn (1 1 1), (1 1 0) and (1 0 0) surfaces, respectively. The shift in the *d*-band centre closer to the Fermi level in the bimetallic NiZn surfaces is consistent with the stronger binding energy observed on the NiZn surfaces compared to the monometallic surfaces [60].

These results suggest that the combination of two weakly active metals (Ni and Zn) gives a highly active bimetallic NiZn catalyst for hydrazine adsorption and activation towards direct hydrazine fuel cell applications. The improved activity of the bimetallic NiZn catalyst may, therefore, be attributed to the beneficial synergistic effects derived from the composition and electronic structure modulation. Further insights into the hydrazine adsorption process on the bimetallic NiZn catalyst was ascertained through the projected density of states (PDOS) and differential charge density isosurface analyses. As shown in Fig. 7a-c, the chemisorption of hydrazine on the bimetallic NiZn catalyst is found to be characterized by strong hybridization between the *d*-orbitals of interacting surface Ni and Zn sites and on the N *p*-orbitals of hydrazine. Consistent with chemisorption, we observed electron density accumulation within the Ni-N and Zn-N bonding regions as shown in Fig. 7d-f. Considering that the charge transfers between hydrazine and the surface is small and that there is no clear trend between charge transfers and the calculated adsorption energies, the differences in the hydrazine adsorption strength to the different surfaces and may also be attributed to the differences in the coordination numbers of the surface Ni and Zn atoms. This invariably dictates adsorption environment at each active site, whereby the low-coordinated Ni sites on the NiZn (1 1 1) surface enables the strongest hydrazine adsorption.

4. Conclusions

In summary, we have performed a comprehensive first-principles dispersion-corrected DFT investigation of hydrazine adsorption on bimetallic NiZn (1 1 1), (1 1 0) (1 0 0) surfaces and compared the results to the monometallic Ni(1 1 1) and Zn(1 0 0) surfaces. The synergistic beneficial effects derived from surface composition and electronic structure modification with Ni and Zn alloying gave rise to more reactive surface sites that bind hydrazine more strongly than the single-component nickel and zinc metal surfaces. It is found that the Ni-terminated (1 1 1) and (1 1 0) NiZn surfaces preferentially bind the hydrazine molecule in a bidentate eclipsed geometry, compared to the Zn-terminated (1 0 0) surface where binding a bidentate gauche adsorption geometry is favoured. The stronger adsorption of hydrazine on the bimetallic NiZn nanocatalyst than the monometallic is shown to be characterised by stronger hybridisation between the *d*-orbitals of the interacting surface sites and the N *p*-orbitals of the hydrazine, which is corroborated by the observed shift in the *d*-band centre closer to the Fermi level. These results should provide new possibilities for the design and development of Ni-Zn alloy catalysts with improved activity and selectivity of hydrazine electro-oxidation in the DHFC.

CRediT authorship contribution statement

R.W.C is responsible for data curation, formal analysis, and writing of original draft. S.R.R performed writing - review and editing. N.Y.D is responsible for funding acquisition, project conceptualization, administration, supervision, and writing - review and editing of manuscript.

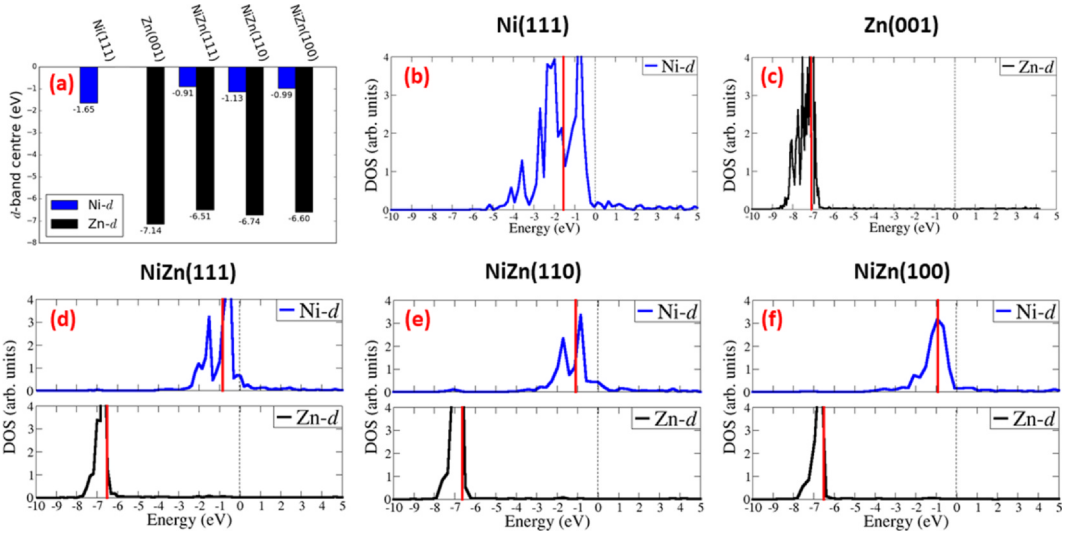

Fig. 6. Calculated *d*-band centre for each of the Ni(1 1 1), Zn(0 0 1) and NiZn(1 1 1), (1 1 0) and (1 0 0) surfaces (a). Ni values are shown in blue, while Zn is in black. The surface DOS for Ni and Zn-*d* for the monometallic catalysts (b-c) and bimetallic NiZn (d-f) are shown, with the *d*-band centre denoted by the continuous red line and the Fermi level by the dashed black line. (For interpretation of the references to colour in this figure legend, the reader is referred to the web version of this article.)

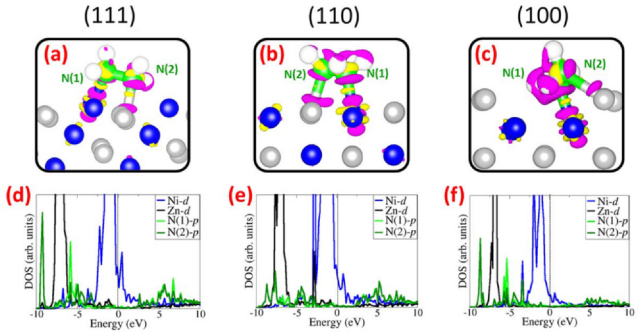

Fig. 7. Differential charge density isosurface contours of most stable hydrazine adsorption to bimetallic NiZn (1 1 1), (1 1 0) and (1 0 0) catalyst surfaces (a-c) - where accumulation is shown in pink and depletion in yellow, by ± 0.003 e/Å^3 respectively. These are followed by the corresponding projected density of states (d-f) for each system.

Declaration of Competing Interest

The authors declare that they have no known competing financial interests or personal relationships that could have appeared to influence the work reported in this paper.

Acknowledgments

This research was funded by the UK's Engineering and Physical Sciences Research Council (EPSRC), grant number EP/S001395/1. R.W.C. acknowledges the College of Physical Sciences and Engineering, Cardiff University for studentship. We also acknowledge the used of computational facilities of the Advanced Research Computing at Cardiff (ARCCA) Division, Cardiff University, and HPC Wales. Information on the data that underpins the results presented here, including how to access them, can be found in the Cardiff University data catalogue at http://doi.org/10.17035/d.2020.0115779666.

Appendix A. Supplementary material

Supplementary data to this article can be found online at https://doi.org/10.1016/j.apsusc.2020.147648.

References

[1] J. Cheng, G. He, F. Zhang, Int. J. Hydrogen Energy 40 (2015) 7348–7360.
[2] U. Lucia, Renew. Sustain. Energy Rev. 30 (2014) 164–169.
[3] S. Suzuki, H. Muroyama, T. Matsui, K. Eguchi, J. Power Sources 208 (2012) 257–262.
[4] N. Fujiwara, Z. Siroma, T. Ioroi, K. Yasuda, J. Power Sources 164 (2007) 457–463.
[5] K. Yamada, K. Asazawa, K. Yasuda, T. Ioroi, H. Tanaka, Y. Miyazaki, T. Kobayashi, J. Power Sources 115 (2003) 236–242.
[6] W.X. Yin, Z.P. Li, J.K. Zhu, H.Y. Qin, J. Power Sources 182 (2008) 520–523.
[7] G.E. Evans, K.V. Kordesch, Science (80-.), 158 (1967) 1148 LP-1152.
[8] T. Sakamoto, K. Asazawa, J. Sanabria-Chinchilla, U. Martinez, B. Halevi, P. Atanassov, P. Strasser, H. Tanaka, J. Power Sources 247 (2014) 605–611.
[9] K. Asazawa, K. Yamada, H. Tanaka, A. Oka, M. Taniguchi, T. Kobayashi, Angew. Chemie 119 (2007) 8170–8173.
[10] J. Sanabria-Chinchilla, K. Asazawa, T. Sakamoto, K. Yamada, H. Tanaka, P. Strasser, J. Am. Chem. Soc. 133 (2011) 5425–5431.
[11] A. Serov, M. Padilla, A.J. Roy, P. Atanassov, T. Sakamoto, K. Asazawa, H. Tanaka, Angew. Chemie Int. Ed. 53 (2014) 10336–10339.
[12] T. Asset, A. Roy, T. Sakamoto, M. Padilla, I. Matanovic, K. Artyushkova, A. Serov, F. Maillard, M. Chatenet, K. Asazawa, H. Tanaka, P. Atanassov, Electrochim. Acta 215 (2016) 420–426.
[13] P. Yang, L. Yang, Q. Gao, Q. Luo, X. Zhao, X. Mai, Q. Fu, M. Dong, J. Wang, Y. Hao, R. Yang, X. Lai, S. Wu, Q. Shao, T. Ding, J. Lin, Z. Guo, Chem. Commun. 55 (2019) 9011–9014.
[14] T. Sakamoto, D. Matsumura, K. Asazawa, U. Martinez, A. Serov, K. Artyushkova, P. Atanassov, K. Tamura, Y. Nishihata, H. Tanaka, Electrochim. Acta 163 (2015) 116–122.
[15] N.V. Rees, R.G. Compton, Energy Environ. Sci. 4 (2011) 1255–1260.
[16] S. De, J. Zhang, R. Luque, N. Yan, Energy Environ. Sci. 9 (2016) 3314–3347.
[17] J. Wang, X.-B. Zhang, Z.-L. Wang, L.-M. Wang, Y. Zhang, Energy Environ. Sci. 5 (2012) 6885–6888.
[18] S.K. Singh, Q. Xu, Chem. Commun. 46 (2010) 6545–6547.
[19] L. He, Y. Huang, X.Y. Liu, L. Li, A. Wang, X. Wang, C.-Y. Mou, T. Zhang, Appl. Catal. B Environ. 147 (2014) 779–788.
[20] S.K. Singh, Q. Xu, Inorg. Chem. 49 (2010) 6148–6152.
[21] K. Aranishi, A.K. Singh, Q. Xu, ChemCatChem 5 (2013) 2248–2252.
[22] L. Xu, N. Liu, B. Hong, P. Cui, D. Cheng, F. Chen, Y. An, C. Wan, RSC Adv. 6 (2016) 31687–31691.
[23] M. Sun, Z. Lu, L. Luo, Z. Chang, X. Sun, Nanoscale 8 (2016) 1479–1484.
[24] Y.-B. He, J.-F. Jia, H.-S. Wu, J. Phys. Chem. C 119 (2015) 8763–8774.
[25] L.-S. Wu, H.-B. Dai, X.-P. Wen, P. Wang, ChemElectroChem 4 (2017) 1944–1949.
[26] Z. Feng, D. Li, L. Wang, Q. Sun, P. Lu, P. Xing, M. An, Electrochim. Acta 304 (2019) 275–281.
[27] Z. Feng, D. Li, L. Wang, Q. Sun, P. Lu, P. Xing, M. An, J. Alloys Compd. 788 (2019) 1240–1245.
[28] N.Y. Dzade, N.H. de Leeuw, J. Phys. Chem. C 122 (2018) 359–370.
[29] N.Y. Dzade, A. Roldan, N.H. de Leeuw, J. Chem. Phys. 139 (2013) 124708.
[30] N.Y. Dzade, A. Roldan, N.H. de Leeuw, Environ. Sci. Technol. 51 (2017) 3461–3470.
[31] M.K. Agusta, H. Kasai, Surf. Sci. 606 (2012) 766–771.
[32] S.S. Tafreshi, A. Roldan, N.Y. Dzade, N.H. de Leeuw, Surf. Sci. 622 (2014) 1–8.
[33] A.T. Hanindriyo, T.B.M.Y.Y. Prawira, M.K. Agusta, R. Maezono, H.K. Dipojono,

Procedia Eng. 170 (2017) 148–153.
[34] G. Kresse, J. Non. Cryst. Solids 192–193 (1995) 222–229.
[35] G. Kresse, J. Furthmüller, Comput. Mater. Sci. 6 (1996) 15–50.
[36] G. Kresse, J. Furthmüller, Phys. Rev. B 54 (1996) 11169–11186.
[37] P.E. Blöchl, Phys. Rev. B 50 (1994) 17953–17979.
[38] G. Kresse, D. Joubert, Phys. Rev. B 59 (1999) 1758–1775.
[39] J.P. Perdew, K. Burke, M. Ernzerhof, Phys. Rev. Lett. 77 (1996) 3865–3868.
[40] H.J. Monkhorst, J.D. Pack, Phys. Rev. B 13 (1976) 5188–5192.
[41] G.W. Watson, E.T. Kelsey, N.H. de Leeuw, D.J. Harris, S.C. Parker, J. Chem. Soc. Faraday Trans. 92 (1996) 433–438.
[42] S. Grimme, J. Antony, S. Ehrlich, H. Krieg, J. Chem. Phys. 132 (2010) 154104.
[43] W. Liu, A. Tkatchenko, M. Scheffler, Acc. Chem. Res. 47 (2014) 3369–3377.
[44] P.O. Bedolla, G. Feldbauer, M. Wolloch, S.J. Eder, N. Dörr, P. Mohn, J. Redinger, A. Vernes, J. Phys. Chem. C 118 (2014) 17608–17615.
[45] I. Hamada, K. Lee, Y. Morikawa, Phys. Rev. B 81 (2010) 115452.
[46] E.S. Menkah, N.Y. Dzade, R. Tia, E. Adei, N.H. de Leeuw, Appl. Surf. Sci. 480 (2019) 1014–1024.
[47] S.S. Tafreshi, A. Roldan, N.H. de Leeuw, Surf. Sci. 637–638 (2015) 140–148.
[48] L.K. Frevel, H.W. Rinn, H.C. Anderson, Ind. Eng. Chem. Anal. Ed. 18 (1946) 83–93.
[49] N.Y. Dzade, ACS Omega 5 (2020) 1025–1032.
[50] N.Y. Dzade, N.H. de Leeuw, Phys. Chem. Chem. Phys. 19 (2017) 27478–27488.
[51] N.Y. Dzade, A. Roldan, N.H. de Leeuw, Phys. Chem. Chem. Phys. 18 (2016) 32007–32020.
[52] K. Kohata, T. Fukuyama, K. Kuchitsu, J. Phys. Chem. 86 (1982) 602–606.
[53] M.K. Agusta, W.A. Diño, M. David, H. Nakanishi, H. Kasai, Surf. Sci. 605 (2011) 1347–1353.
[54] M.K. Agusta, M. David, H. Nakanishi, H. Kasai, Surf. Sci. 604 (2010) 245–251.
[55] Z. Deng, X. Lu, Z. Wen, S. Wei, Y. Liu, D. Fu, L. Zhao, W. Guo, Phys. Chem. Chem. Phys. 15 (2013) 16172–16182.
[56] F. Calle-Vallejo, J.I. Martínez, J.M. García-Lastra, P. Sautet, D. Loffreda, Angew. Chemie Int. Ed. 53 (2014) 8316–8319.
[57] B. Hammer, J. K. B. T.-A. in C. Nørskov. In: Impact of Surface Science on Catalysis, Academic Press, 2000, vol. 45, pp. 71–129.
[58] B. Hammer, J.K. Norskov, Nature 376 (1995) 238–240.
[59] J.K. Nørskov, F. Abild-Pedersen, F. Studt, T. Bligaard, Proc. Natl. Acad. Sci. 108 (2011) 937 LP-943.
[60] X. Liu, W. An, Y. Wang, C.H. Turner, D.E. Resasco, Catal. Sci. Technol. 8 (2018) 2146–2158.